ROYAL SOCIETY
OF CHEMISTRY

PAPER

Check for updates

Co/Ni-polyoxotungstate photocatalysts as precursor materials for electrocatalytic water oxidation†

Robin Güttinger, [ID] ‡ Giann Wiprächtiger, [ID] ‡ Olivier Blacque [ID] and Greta R. Patzke [ID] *

An open-core cobalt polyoxometalate (POM) $[(A\text{-}\alpha\text{-}SiW_9O_{34})Co_4(OH)_3(CH_3COO)_3]^{8-}$ **Co(1)** and its isostructural Co/Ni-analogue $[(A\text{-}\alpha\text{-}SiW_9O_{34})Co_{1.5}Ni_{2.5}(OH)_3(CH_3COO)_3]^{8-}$ **CoNi(2)** were synthesized and investigated for their photocatalytic and electrocatalytic performance. **Co(1)** shows high photocatalytic O_2 yields, which are competitive with leading POM water oxidation catalysts (WOCs). Furthermore, **Co(1)** and **CoNi(2)** were employed as well-defined precursors for heterogeneous WOCs. Annealing at various temperatures afforded amorphous and crystalline $CoWO_4$- and $Co_{1.5}Ni_{2.5}WO_4$-related nanoparticles. $CoWO_4$-related particles formed at 300 °C showed substantial electrocatalytic improvements and were superior to reference materials obtained from co-precipitation/annealing routes. Interestingly, no synergistic interactions between cobalt and nickel centers were observed for the mixed-metal POM precursor and the resulting tungstate catalysts. This stands in sharp contrast to a wide range of studies on various heterogeneous catalyst types which were notably improved through Co/Ni substitution. The results clearly demonstrate that readily accessible POMs are promising precursors for the convenient and low-temperature synthesis of amorphous heterogeneous water oxidation catalysts with enhanced performance compared to conventional approaches. This paves the way to tailoring polyoxometalates as molecular precursors with tuneable transition metal cores for high performance heterogeneous electrocatalysts. Our results furthermore illustrate the key influence of the synthetic history on the performance of oxide catalysts and highlight the dependence of synergistic metal interactions on the structural environment.

1. Introduction

Sunlight-driven splitting of water into hydrogen and oxygen, also known as artificial photosynthesis, is among the most direct and elegant one-step concepts for renewable energy sources.[1] However, the development of efficient and noble-metal free water oxidation catalysts (WOCs) for this complex four electron transfer process is still a crucial bottleneck of artificial photosynthesis.[2] A variety of approaches to WOC design have been reported, and in many of them the cuboidal $\{CaMn_4O_5\}$ core of nature's photosystem II is a central motif.[3] Recently, several transition metal WOCs with cubane-related cores have been reported.[4–10]

Polyoxometalates (POMs) are promising WOC candidates, because they combine robustness and structural versatility with the capability of undergoing rapid, reversible, and stepwise

multi-electron transfer reactions, and we also refer to key review articles here.[11–16] Among the attractive and low cost 3d transition metal water splitting catalysts, cobalt-based homogeneous catalysts and POMs keep attracting intense attention.[17–22] Specifically, Co-POMs have recently been applied as co-catalysts on photoanodes or for enhanced performance in composite systems.[23–28].

The coordination of multiple metal centers between two or more lacunary POM units has proven a powerful and quite flexible catalytic motif, such as in the OEC-related $[Mn_3^{III}Mn^{IV}O_3(CH_3COO)_3(SiW_9O_{34})]^{6-}$ with a mixed-valent $\{Mn_4\}$ core.[29] Although many POMs have wide operational stability windows, they can undergo leaching of heteroatoms/transition metals to form active nanoscale oxide catalysts, especially during electrochemical water oxidation.[30,31] This gives rise to ongoing and challenging speciation studies.[32]

Recently, the performance of an amorphous sandwich-type Co-based POM WOC was first enhanced by annealing at 400 °C to form $CoWO_4$ nanoparticles, which outperformed analogous electrocatalysts obtained *via* precipitation routes.[33] Along these lines, mixed-metal manganese cubane[34] and Ni–Zn cubane-like[35] precursors were further applied to enhance the

Department of Chemistry, University of Zurich, Winterthurerstrasse 190, CH-8057 Zurich, Switzerland. E-mail: greta.patzke@chem.uzh.ch; Web: http://www.patzke.ch

† Electronic supplementary information (ESI) available. See DOI: 10.1039/d0ra10792a

‡ These authors contributed equally to this work.

performance of oxide WOCs. These findings show that synthetic methods and underlying mechanisms[36] are an important step in WOC optimization,[37–39] and that a certain extent of pre-organization of the metal centers in the precursor is beneficial for higher catalytic activity.[40] To this end, we systematically explored synthesis-activity relationships with a series of studies on spinel-type Co_3O_4 catalysts, starting with *in situ* PXRD monitoring of temperature-dependent hydrothermal Co_3O_4 formation mechanisms.[41] Next, we revealed the preparation-dependent properties of Co_3O_4 WOCs in different test assays,[42] and studies of their microwave-assisted synthesis further confirmed the crucial role of synthetic pathways for the catalytic performance.[43]

POM as oxide precursors have enabled the efficient synthesis of CoO_x electrocatalysts[44] or of ultrafine transition metal-clusters,[45] as well as inspirational studies on transformation pathways of pre-organized metal centers into structural features of the resulting multinary heterogeneous catalysts.[46,47] Recent trends further employed POMs as versatile metal sources for carbide-, phosphide- and sulphide-based water splitting electrocatalysts.[48–50] All in all, the complexity of such precursor-properties relations remains to be fully explored and understood for efficient WOC design.

Another crucial principle in the optimization of transition metal catalysts are synergistic effects between mixed metal centers, such as the widely studied Ni/Fe interactions in WOCs.[51–53] In comparison, Co/Ni-interactions in oxygen evolution and other catalysts are far more diverse and controversial. Mixed heterogeneous Co/Ni-oxide electrocatalysts have been studied for several decades[54] and were frequently reported to be favourable over binary systems.[55–57] However, later studies on mixed Co/Ni-hydroxides pointed to either productive[58] or adverse[59] effects, or to no significant interactions in the case of oxides at all.[60] Although Co/Ni synergisms were recently observed for sulphide[61] and phosphide[62] water splitting electrocatalysts, their understanding is still empirical to a large extent and modelling studies are now being undertaken.[62] Even less is known about the effect of Co/Ni-substitution on molecular WOCs and other catalysts. In our own work, for example, we have observed drastic contrasts between the notable improvement of solid CoNCN WOCs through Ni-doping[63] *vs.* detrimental effects on molecular $\{Co(\text{II})_4O_4\}$ cubane WOCs.[64] Similar adverse Co/Ni-interactions have been reported for other molecular systems.[65] Generally, a wide range of further studies is now needed to explore the role of materials type, preparative method and test conditions (photo- *vs.* electrochemistry) in the performance of Co/Ni-based catalysts. These widely unresolved questions concerning the prediction and explanation of Co/Ni-interactions inspired us herein to first investigate molecular photocatalyst performance with respect to Ni introduction, followed by its effect on the solid electrocatalysts obtained from such molecular precursors.

To this end, we selected Co/Ni-POMs as attractive and comprehensive models to investigate (a) Co/Ni interactions in molecular WOCs *vs.* (b) those in oxide-based catalysts, while (c) exploring the benefits of POM precursors for oxide WOCs.

To this end, we targeted $CoWO_4$ with favourable 500–650 nm light absorption properties that was also reported as an effective and noble metal-free WOC at low overpotential.[66] Furthermore, $CoWO_4$ performance was found to depend on crystallinity[67] with amorphous $CoWO_4$ being superior to its crystalline form, along the lines of self-repairing CoPi films.[68–70] However, little is still known about the electrocatalytic performance and other applications of mixed Co/Ni-tungsten oxides.[71,72] Binary $CoWO_4$ and $NiWO_4$, for example, display better electrochemical performance in water oxidation than $NiCo_2O_4$ spinels.[72] While mixed $(Co, Ni)WO_4$ materials are attractive for supercapacitor development,[73,74] no synergistic benefits were reported for their use in photocatalytic methylene blue degradation.[75]

We therefore newly investigated the influence of Ni-doping on the performance of $CoWO_4$-related water oxidation catalysts, which were obtained from crystallographically well-defined, bio-inspired M_4-POMs with an exposed metal core architecture. While Ni-containing POMs were reported to be stable and active for water oxidation,[76,77] their potential as mixed metal precursors for heterogeneous WOCs still needs to be explored. To this end, we synthesized and characterized $[(A-\alpha-SiW_9O_{34})Co_4(OH)_3(CH_3COO)_3]^{8-}$ **Co(1)** together with its isostructural analogue $[(A-\alpha-SiW_9O_{34})Co_{1.5}Ni_{2.5}(OH)_3(CH_3COO)_3]^{8-}$ **CoNi(2)**.[78] First, both POMs were compared with respect to their respective photo- and electrocatalytic water oxidation activity. Moreover, they were used as annealing precursors to form $CoWO_4$- and mixed $(Co,Ni)WO_4$-related electrocatalysts, and **Co(1)** was found to be an efficient precursor at temperatures as low as 300 °C.

2. Experimental

2.1 Materials

All chemicals were used as purchased without purification. The lacunary precursor $Na_{10}[A-\alpha-SiW_9O_{34}]\cdot19H_2O$ was synthesized as previously described.[79]

2.2 Physical methods

Attenuated total reflectance Fourier-transform (ATR-FT-IR) spectra were recorded on a Bruker Vertex 70 spectrometer equipped with a Platinum ATR accessory containing a diamond crystal. UV/Vis spectra were recorded on a Lambda 650 S PerkinElmer UV-visible spectrometer in the range of 200–800 nm using a Quartz SUPRASIL precision cell (10 mm). Raman spectroscopy was recorded with a Renishaw inVia Qontor confocal Raman microscope equipped with a diode laser (785 nm). Thermogravimetric analyses were performed on a Netzsch STA 449C between 24 and 600 °C with a heating rate of 10 K min^{-1} in N_2 atmosphere and Al_2O_3 crucible. PXRD patterns were recorded on a STOE STADI P diffractometer (transmission mode, Ge monochromator) with Cu or Mo radiation. XPS analysis was performed using a PhI 5000 VersaProbe spectrometer (ULVAC-PHI, Inc.) equipped with a 180° spherical capacitor energy analyzer and a multi-channel detection system with 16 channels. Spectra were acquired at a base pressure of 5×10^{-8} Pa using a focused scanning monochromatic Al-K_{α} source (1486.6 eV) with a spot size of 200 μm and 50 W. The instrument was

run in the FAT analyzer mode with electrons emitted at 45° to the surface normal. Pass energy used for survey scans was 187.85 eV and 46.95 eV for detail spectra. Charge neutralisation utilizing both a cool cathode electron flood source (1.2 eV) and very low energy Ar^+ ions (10 eV) was applied throughout the analysis.

Visible-light-driven water oxidation was first monitored in solution using an oxygen sensor (OX-N) Clark electrode from Unisense. Constant temperature was maintained with a mineral insulated thermosensor (2 mm tip diameter, TP2000, Unisense). Second, O_2 evolution was measured in the headspace of the vial using an Agilent Technologies 7820A gas chromatograph with helium as the carrier gas and a 3 m × 2 mm packed molecular sieve 13 × 80–100 column to separate O_2 and N_2. The oven was operated isothermally at 100 °C. The analysis of the headspace was performed by taking 100 μL samples with a Hamilton (1825 RN) gas-tight microliter syringe. Gases were detected using a thermal conductivity detector (Varian) operated at 200 °C.

Cyclic voltammetry (CV) measurements were performed on a Metrohm 797 VA Computrace instrument with a platinum electrode (Metrohm AG, 2 mm diameter) as a working electrode, Ag/AgCl reference electrode (sat. KCl, 0.197 V *vs.* NHE) and platinum plate (Metrohm AG) counter electrode. Prior to all measurements, solutions were deaerated with Ar for 15 min. The platinum working electrode was polished between runs with alumina slurry, thoroughly rinsed with water and dried under ambient conditions. The platinum plate was washed in a nitric acid/hydrogen peroxide (1 : 1) solution for 5 min and dried with N_2. The working electrodes were produced by dispersing 5 mg of the sample in 100 μL of H_2O, applying 40 μL of this dispersion on 1 cm² fluorine doped tin oxide (FTO), and drying the electrodes at 80 °C for 30 min before covering with 10 μL Nafion 1% solution.

2.3 $K_5Na_3[(A-\alpha-SiW_9O_{34})Co_4(OH)_3(CH_3COO)_3] \cdot 15H_2O$ (1)[78]

$Co(CH_3COO)_2 \cdot 4H_2O$ (0.712 g, 2.86 mmol) was dissolved in an aqueous solution of potassium acetate (0.5 M, 16 mL), adjusted to pH 8 with HCl and stirred for 15 min. $Na_{10}[A-\alpha-SiW_9O_{34}] \cdot 19H_2O$ (1.977 g, 0.7 mmol) was added and stirred for 45 min at 40 °C. The mixture was then cooled to room temperature and placed in the fridge for 10 min. The purple suspension was centrifuged, filtered and left at room temperature for slow evaporation. After three weeks purple crystals were collected and analysed by FT-IR and Raman spectroscopy, powder X-ray diffraction, ICP-MS, EDX and ESI-MS. (yield 0.34 g, 15% based on tungsten). FT-IR: $\tilde{\nu}$ = 1598 (m), 1552 (m), 1415 (m), 1350 (w), 979 (w), 931 (m), 883 (s), 792 (s), 665 (s), 514 (s), 451 cm⁻¹(m). ESI-MS: 879.3938 $[M-(CH_3COO) + 5H^+]^{3-}$.

2.4 $K_5Na_3[(A-\alpha-SiW_9O_{34})Co_{1.5}Ni_{2.5}(OH)_3(CH_3COO)_3] \cdot 16H_2O$ (2)

$Co(CH_3COO)_2 \cdot 4H_2O$ (0.352 g, 1.41 mmol) and $Ni(CH_3COO)_2 \cdot 4H_2O$ (0.366 g, 1.47 mmol) were dissolved in an aqueous solution of potassium acetate (1 M, 16 mL), adjusted to pH 8 with HCl and stirred for 15 min. $Na_{10}[A-\alpha-SiW_9O_{34}] \cdot 19H_2O$ (1.513 g, 0.53 mmol) was added and stirred for 45 min at 40 °C. The mixture was then cooled to room temperature and placed in the fridge for 10 min. The purple suspension was centrifuged, filtered and left at room temperature for slow evaporation. After two weeks light purple crystals were collected and analysed by FT-IR and Raman spectroscopy, powder X-ray diffraction, ICP-MS, EDX and ESI-MS (yield 0.23 g, 13% based on tungsten). FT-IR: $\tilde{\nu}$ = 1606 (m), 1556 (m), 1421 (m), 1350 (w), 979 (w), 941 (m), 883 (s), 802 (s), 665 (s), 514 (s), 451 cm⁻¹ (m). ESI-MS: 876.7113 $[M-(CH_3COO) + 5H^+]^{3-}$.

2.4.1 CoW200. $K_5Na_3[(A-\alpha-SiW_9O_{34})Co_4(OH)_3(CH_3COO)_3] \cdot 15H_2O$ (0.043 g) was added into a crucible and placed in a furnace which was heated to 200 °C with a ramping temperature of 5 °C min⁻¹ and annealed for 1 h to yield 0.04 g. After cooling down to room temperature, the violet compound was analysed with FT-IR and Raman spectroscopy as well as PXRD. FT-IR: $\tilde{\nu}$ = 1560 (m), 1404 (m), 1338 (w), 1116 (w), 987 (w), 939 (m), 865 (s), 779 (s), 661 (s), 524 cm⁻¹ (m).

2.4.2 CoW300. $K_5Na_3[(A-\alpha-SiW_9O_{34})Co_4(OH)_3(CH_3COO)_3] \cdot 15H_2O$ (0.087 g) was added into a crucible and placed in a furnace which was heated to 300 °C with a ramping temperature of 5 °C min⁻¹ and annealed for 1 h to yield 0.08 g. After cooling down to room temperature the black compound was analysed by FT-IR and Raman spectroscopy as well as PXRD. FT-IR: $\tilde{\nu}$ = 1564 (w), 1404 (w), 1340 (w), 1128 (w), 939 (m), 852 (s), 771 (s), 702 (s), 538 cm⁻¹ (m).

2.4.3 CoW400. $K_5Na_3[(A-\alpha-SiW_9O_{34})Co_4(OH)_3(CH_3COO)_3] \cdot 15H_2O$ (0.305 g) was added into a crucible and placed in a furnace which was heated to 400 °C with a ramping temperature of 5 °C min⁻¹ and annealed for 1 h to yield 0.27 g. After cooling down to room temperature the grey compound was analysed by FT-IR and Raman spectroscopy as well as PXRD. FT-IR: $\tilde{\nu}$ = 1128 (m), 929 (w), 823 (s), 790 (s), 599 (s), 518 (s), 460 cm⁻¹ (m).

2.4.4 CoW500. $K_5Na_3[(A-\alpha-SiW_9O_{34})Co_4(OH)_3(CH_3COO)_3] \cdot 15H_2O$ (0.09 g) was added into a crucible and placed in a furnace which was heated to 500 °C with a ramping rate of 5 °C min⁻¹ and annealed for 1 h to yield 0.08 g. After cooling down to room temperature the dark blue compound was analysed with FT-IR and Raman spectroscopy as well as PXRD. FT-IR: $\tilde{\nu}$ = 1114 (m), 931 (w), 819 (s), 599 (s), 516 (s), 462 cm⁻¹ (s).

2.4.5 CoNi200. $K_5Na_3[(A-\alpha-SiW_9O_{34})Co_{1.5}Ni_{2.5}(OH)_3(CH_3COO)_3] \cdot 16H_2O$ (0.021 g) was added into a crucible and placed in a furnace which was heated to 200 °C with a ramping rate of 5 °C min⁻¹ and annealed for 1 h to yield 0.02 g. After cooling down to room temperature the purple compound was analysed with FT-IR and Raman spectroscopy as well as PXRD. FT-IR: $\tilde{\nu}$ = 1562 (m), 1407 (m), 1344 (w), 1122 (w), 981 (w), 933 (m), 858 (s), 798 (s), 671 (s), 520 cm⁻¹ (m).

2.4.6 CoNi300. $K_5Na_3[(A-\alpha-SiW_9O_{34})Co_{1.5}Ni_{2.5}(OH)_3(CH_3COO)_3] \cdot 16H_2O$ (0.087 g) was added into a crucible and placed in a furnace which was heated to 300 °C with a ramping rate of 5 °C min⁻¹ and annealed for 1 h to yield 0.08 g. After cooling down to room temperature the black compound was analysed with FT-IR and Raman spectroscopy as well as PXRD. FT-IR: $\tilde{\nu}$ = 1569 (w), 1404 (w), 1128 (w), 933 (m), 838 (s), 788 (s), 711 (s), 540 cm⁻¹ (m).

2.4.7 CoNi400. $K_5Na_3[(A-\alpha-SiW_9O_{34})Co_{1.5}Ni_{2.5}(OH)_3(CH_3COO)_3]\cdot16H_2O$ (0.114 g) was added into a crucible and placed in a furnace which was heated to 400 °C with a ramping rate of 5 °C min^{-1} and annealed for 1 h to yield 0.10 g. After cooling down to room temperature the grey compound was analysed with FT-IR and Raman spectroscopy as well as PXRD. FT-IR: $\tilde{\nu}$ = 1107 (w), 941 (m), 858 (s), 813 (s), 773 (s), 725 cm^{-1} (s).

2.4.8 CoNi500. $K_5Na_3[(A-\alpha-SiW_9O_{34})Co_{1.5}Ni_{2.5}(OH)_3(CH_3COO)_3]\cdot16H_2O$ (0.057 g) was added into a crucible and placed in a furnace which was heated to 500 °C with a ramping rate of 5 °C min^{-1} and annealed for 1 h to yield 0.05 g. After cooling down to room temperature the dark green compound was analysed with FT-IR and Raman spectroscopy as well as PXRD. FT-IR: $\tilde{\nu}$ = 1116 (m), 933 (w), 821 (s), 605 (s), 509 (s), 466 cm^{-1} (m).

2.4.9 Reference CoWO$_4$. An aqueous solution of Na_2WO_4 (0.1 M, 10 mL) was added dropwise to a $Co(NO_3)_2$ solution (0.1 M, 10 mL) under vigorous stirring. The precipitate was rinsed with water after centrifugation and dried overnight in the oven (40 °C). The collected precipitate was added into a crucible and placed in a furnace which was heated to 300 °C with a ramping rate of 5 °C min^{-1} and annealed for 1 h.[66]

3. Results and discussion

3.1 Synthesis and analytical characterization

$[(A-\alpha-SiW_9O_{34})Co_4(OH)_3(CH_3COO)_3]^{8-}$ **Co(1)** was synthesized by mixing stoichiometric amounts of the precursor[80] $Na_{10}[A-\alpha-SiW_9O_{34}]$ and cobalt acetate in potassium acetate (0.5 M, pH 8) solution with moderate heating. After cooling to room temperature, the mixture was filtered and any insoluble residue was removed, whereupon crystals were obtained after slow evaporation.

FT-IR analysis shows characteristic bands for the bidentate bridging acetate ligands in the range of 1650 to 1400 cm^{-1}. Additional bands related to the Keggin structure appear around 934 (ν_{as}(W–O$_d$)), 883 (ν_{as}(W–O$_b$)) and 740 cm^{-1} (ν_{as}(W–O$_c$)) (Fig. S1†).[81] Raman spectra show representative peaks at 959 cm^{-1} (ν_{as}(W–O$_d$)), 939 cm^{-1} (ν_{as}(W–O$_b$–W)) and 891 cm^{-1} (ν_{as}(W–O$_b$–W)) of Keggin-type POMs (see below, Fig. 3).[80,82] Further analysis with powder X-ray diffraction (PXRD) of **Co(1)** (Fig. S13†) showed crystalline purity when compared to the calculated pattern (CCDC-619251).

The all-cobalt POM **Co(1)** was further mixed with nickel acetate in a stoichiometric 1 : 1 ratio under slightly changed reaction conditions. The filtration process after the synthesis had to be extended, but phase pure crystals were obtained after slow evaporation and yielded $[(A-\alpha-SiW_9O_{34})Co_{1.5}Ni_{2.5}(OH)_3(CH_3COO)_3]^{8-}$ **CoNi(2)**. FT-IR analysis confirms the presence of the bridging acetate ligands as well as the characteristic bands of the Keggin-type POM at around 941 (ν_{as}(W–O$_d$)), 883 (ν_{as}(W–O$_b$)) and 748 cm^{-1} (ν_{as}(W–O$_c$)) (Fig. S2†).[81] The PXRD pattern confirmed phase purity of **CoNi(2)** and its isostructural relation to **Co(1)**, and only small peak shifts of the peaks towards higher angles are visible which corresponds to a smaller unit cell, as expected (Fig. S16†). Raman spectra show the same representative peaks as observed for **Co(1)** (see below, Fig. 3).

UV-Vis monitoring of **Co(1)** in borate buffer (0.1 M, pH 8) during 24 h showed no significant changes in the spectra. This indicates that **Co(1)** is stable and does not leach any Co^{2+} ions into the solution under these operational conditions (Fig. S6†). According to previous studies,[78] the tetracobalt core is stabilized by an all-inorganic tungstosilicate, as well as bridged by three μ_2-acetate ligands (Fig. 1). All Co^{II} centers of the $\{Co_4^{II}O_3\}$ core are in an octahedral environment and the whole unit displays C_S symmetry, with a mirror plane through the Co$_3$, Co$_2$ and Si atoms. Three Co^{II} centers are connected to the lacunary side of the $[\alpha-SiW_9O_{34}]^{10-}$ POM. The Co–Co distances fall in the range of 2.978(1)–3.711(2) Å and the Co–O distances range from 2.043(0) to 2.117(7) Å, respectively.[78] We confirmed the presence of these structural features in **Co(1)** with single crystal X-ray diffraction analyses giving rise to analogous values (data not shown). The tetracobalt core displays features related to the natural OEC with Mn–Mn distances in the range of 2.8–3.3 Å,[3] and the acetate-bridged cobalt centers relate it to previously reported $\{Co_4^{II}O_4\}$ cubanes.[6,83,84]

In addition, mixed nickel/cobalt acetate precursors yielded the iso-structural **CoNi(2)** with a Co : Ni ratio around 1.5 : 2.5. This ratio was confirmed with EDX, ICP-MS as well as with XPS measurements (Fig. S20, Tables S3, S11 and S12†). The measured Co/Ni : W as well as Co/Ni : Si ratios correspond to the respective calculated ratios of 4 : 9 and 4 : 1 (Tables S11 and S12†). Further HR-ESI-MS analyses showed slightly different masses for the corresponding [M-(CH$_3$COO) + 5H$^+$]$^{3-}$ fragment which correspond to the isotopic distributions of Co and Ni (Fig. S29–S32†). Both POMs display good agreement between experimental PXRD patterns and the respective calculated data (Fig. S13, S15, Tables S1 and S2†). The PXRD pattern of **CoNi(2)** showed a slight shift of the peaks compared to the calculated reference pattern of **Co(1)** (CCDC-619251). Further comparison with the calculated PXRD pattern (Fig. S14†) of the lacunary Ni-analogue $[(A-\alpha-SiW_9O_{34})Ni_4(CH_3COO)_3]^{5-}$ that crystallizes in a different space group[85] ($P\bar{3}1c$ other than $P2_1/m$ for **Co(1)**[78]) clearly showed that the phase pure **CoNi(2)** sample is iso-structural with **Co(1)**, which was also confirmed by Rietveld refinement results (Fig. S15†).
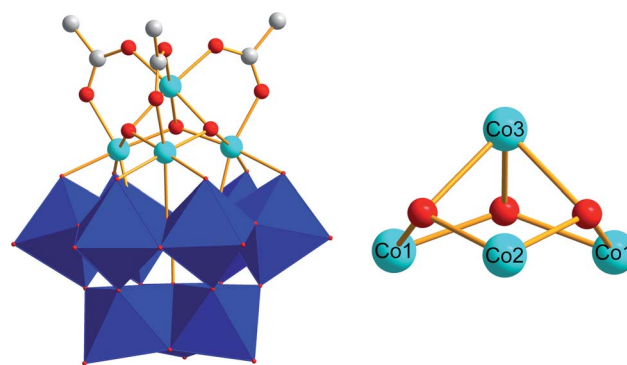

Fig. 1 Polyhedral and ball-and-stick representation of the $[(A-\alpha-SiW_9O_{34})Co_4(OH)_3(CH_3COO)_3]^{8-}$ polyanion **Co(1)** (blue octahedra: $\{WO_6\}$; light blue spheres: Co; white spheres: C; red spheres: O; image derived from CCDC-619251).[71]
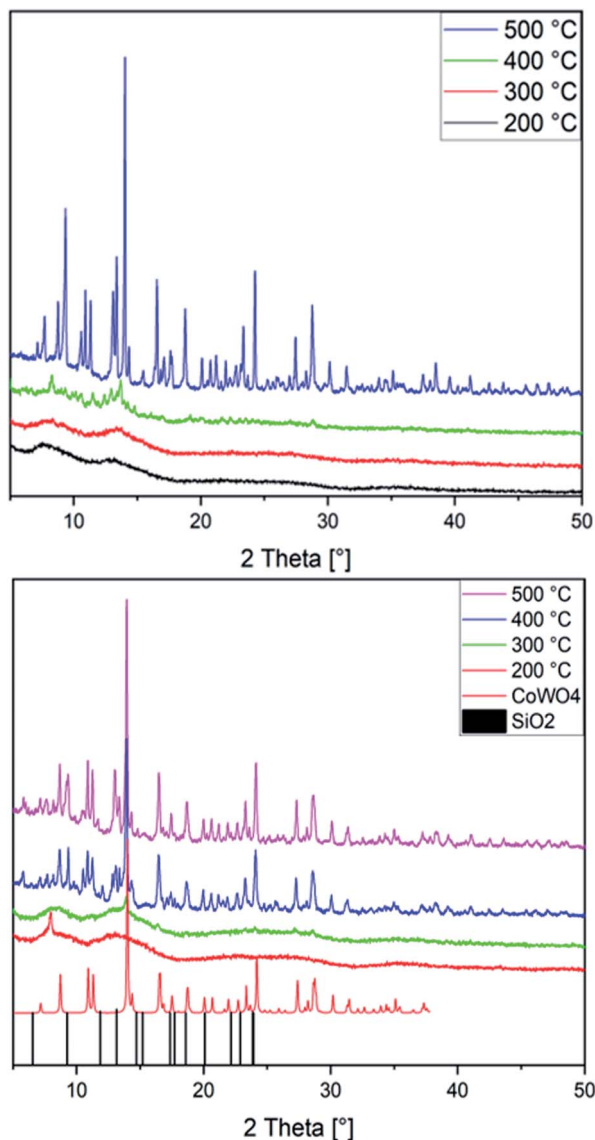
Fig. 2 PXRD patterns of the **CoNiX00** (top) and **CoWX00** (bottom) series annealed at 200 °C (black) up to 500 °C (purple; CoWO$_4$: CCDC-619251, SiO$_2$: PDF No. 12-0711).

CoWO$_4$ nanoparticles keep attracting intense interest as target for synthetic studies, *e.g. via* precipitation,[86,87] hydrothermal[88,89] or spray pyrolysis routes.[90] Here, we newly used both **Co(1)** and **CoNi(2)** as precursors for annealing in air at temperatures ranging from 200 to 500 °C. With a ramping rate of 5 °C min^{-1} and an annealing time of 1 h, amorphous and crystalline nanoparticles were formed. PXRD patterns show the presence of an amorphous material up to 300 °C, while at temperatures of 400 °C and above a crystalline material emerges from both precursor types (Fig. 2). The majority of the peaks in patterns recorded with MoK$_\alpha$ radiation can be assigned to monoclinic CoWO$_4$ (PDF 01-072-0479) and its Ni-doped analogue, in line with previous studies.[86,89,90] While a preceding study on the use of sandwich-type [Co$_4$(H$_2$O)$_2$(-PW$_9$O$_{34}$)$_2$]$^{10-}$ POMs for cobalt tungstate catalysts reported on the formation of Na$_2$W$_2$O$_7$ as a secondary phase at annealing

temperatures of 500 °C,[33] we did not find any indication for major W- or Co-based side products. Extensive database search provided SiO$_2$ (PDF No. 12-0711) as the closest match to account for the minority phases observed here.

Given that SiO$_2$ is widely known as a catalyst support material rather than as active phase, we further considered cobalt tungstosilicates a more reasonable precursor choice than tungstophosphates. The latter may eventually give rise to highly catalytically active cobalt phosphate-related side products. Indeed, phosphorus peaks had been shown in the EDS spectra of the most active amorphous cobalt tungstate catalyst obtained from [Co$_4$(H$_2$O)$_2$(PW$_9$O$_{34}$)$_2$]$^{10-}$ at 400 °C in the above-mentioned study, but no further discussion of the influence of P heteroatoms on the structure or catalytic performance was provided.[33]
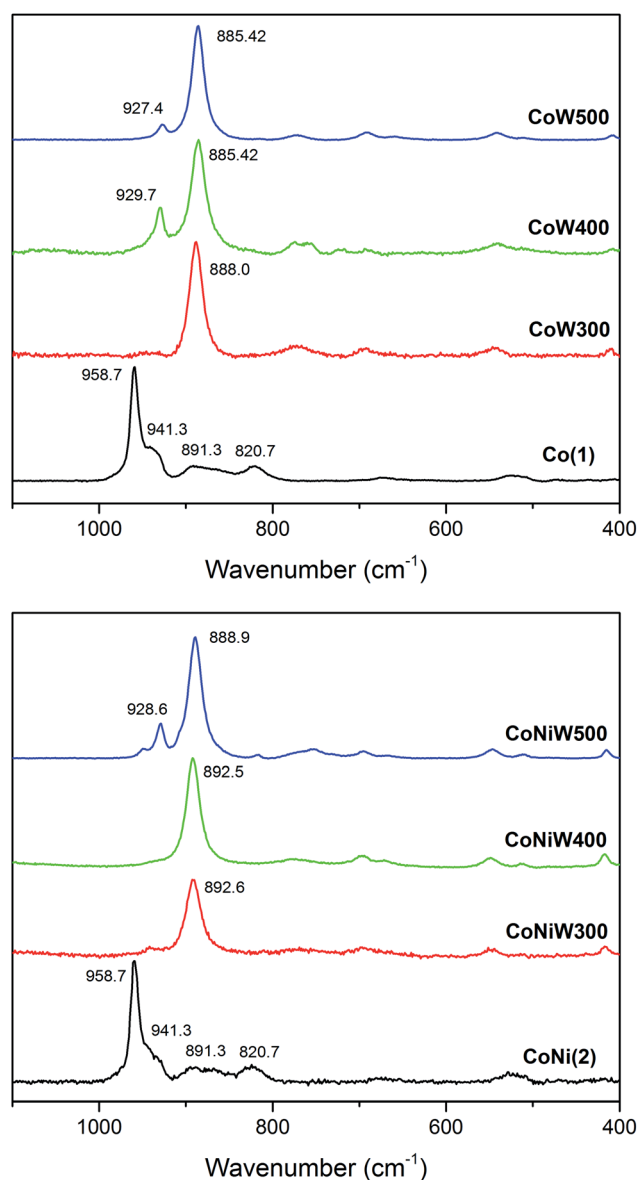

Fig. 3 Raman spectra of **Co(1)** together with the **CoW300/400/500** series (top; black/red/green/blue) and of compound **CoNi(2)** with the **CoNiW300/400/500** series (bottom; black/red/green/blue).
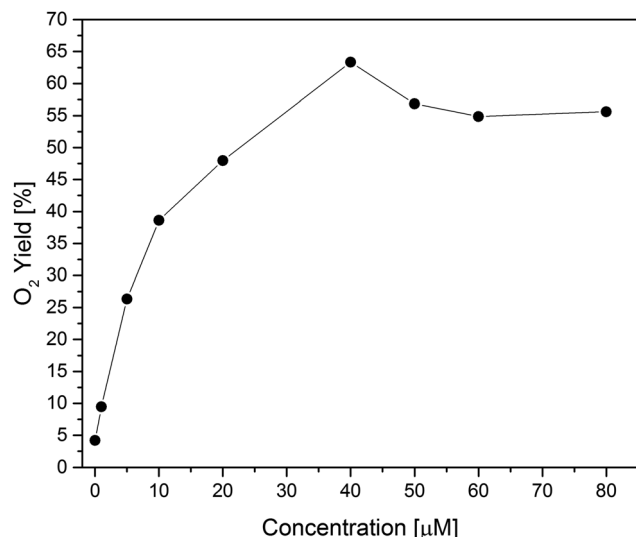
Fig. 4 Photocatalytic oxygen yield *vs.* WOC concentration for **Co(1)**.

The Raman spectra of crystalline **CoW300/400/500** are in good agreement with the reported pattern of CoWO₄ (Fig. 3).[91] The most intense band located at 885 cm^{-1} corresponds to the stretching W–O vibration and is shifted to higher frequencies upon mixing with Ni. The small band around 929 cm^{-1} can be attributed to the symmetric stretching mode of the terminal (W=O) bond.[66,92] The amorphous **CoW300** and **CoNi300/400** samples show a small blue shift of the main W–O stretching vibration compared to the crystalline samples. This is a sign of compressive stress, indicating that the respective Co–Co and Co–Ni distances are smaller compared to the crystalline samples.[92] The weak peak around 500 cm^{-1} can be assigned to the minority phase related to SiO₂.[93]

EDX mappings of the different **CoW*X*00** and **CoNiW*X*00** tungsten oxides show a homogenous distribution of Co/Ni, W and O in all samples (Fig. S23–S28 and Tables S5–S10†) and the elemental ratios of the **CoW*X*00** series are in line with CoWO₄.

3.2 Photo- and electrocatalytic water oxidation activity of Co(1) and CoNi(2)

3.2.1 Photocatalytic activity of Co(1) and CoNi(2). The photocatalytic water oxidation activities of **Co(1)** and **CoNi(2)**

were investigated in a borate buffer solution (0.1 M, pH 8, 8 mL) with [Ru(bpy)₃]$^{2+}$ (1 mM) as photosensitizer (PS) and Na₂S₂O₈ (5 mM) as sacrificial electron acceptor under irradiation at 470 nm. O₂ evolution was monitored by GC-MS to determine the overall TON and with a Clark electrode to determine the initial TOF.

The general mechanism of photocatalytic water oxidation using the [Ru(bpy)₃]$^{2+}$/S₂O₈$^{2-}$ assay has been studied in numerous works, which are summarized in recent topical reviews,[94] including POM water oxidation catalysts.[15] In short, a wide range of studies confirmed that the photoexcited state [Ru(bpy)₃]$^{2+*}$ is quenched by S₂O₈$^{2-}$ to generate [Ru(bpy)₃]$^{3+}$ along with SO₄$^{•-}$, which can bring forward another molecule of [Ru(bpy)₃]$^{3+}$. To finally generate O₂, four holes are first transferred to the POM-WOC *via* four [Ru(bpy)₃]$^{3+}$ equivalents, and the so oxidized POM catalyst can then further oxidize two water molecules. The precise local mechanisms at the active transition metal centers of different POM-WOCs are subject to advanced theoretical studies and further investigations, and they may vary individually for each POM type.[95]

For photocatalytic performance evaluation, first **Co(1)** was tested in different buffer solutions and pH values to explore the optimal water oxidation conditions. Borate buffer (0.1 M, pH 8) led to the best performance ahead of borate buffer (0.1 M, pH 9) and phosphate buffer (0.1 M, pH 7). No activity was observed in acetate buffer (0.1 M, pH 4.75) (Fig. S33†).

Second, concentration screening of **Co(1)** was performed to further optimize the working conditions (Fig. 4, S34 and S35†). Although water oxidation is generally thermodynamically favorable at higher pH values, performances at pH 8 were found to be superior to pH 9,[96] in line with other studies.[6] The maximum O₂ yield of 63% was achieved with 40 μM of **Co(1)**. Compared to other reported Co- or Ni-based POMs, this O₂ yield is competitive for the applied photocatalytic assay (Table 1). In comparison, the Mn-based analogue [Mn₃^{III}Mn^{IV}O₃(CH₃COO)₃(A-α-SiW₉O₃₄)]$^{6-}$ exhibited a rather low photocatalytic performance with 3% oxygen yield.[29]

In Table 1, TON, TOF and O₂ yields are compared to several previously reported POM-WOCs. TONs were increasing with reduced catalyst concentrations, reaching a value of 235 at a catalyst concentration of 1 μM (Table S13†). In the absence of **Co(1)**, a background O₂ evolution of 0.83 μmol was detected, which corresponds to 4% O₂ yield. Additionally, a reference

Table 1 TON, TOF [s^{-1}], and O₂ yield of topically related, selected POM WOCs

Catalyst	TON	TOF	O₂ yield/%	Ref.
Co(1)	40	0.5	63	This work
CoNi(2)	16	0.2	26	This work
[a][(SiW₉O₃₄)₂Co₈(OH)₆(H₂O)₂(CO₃)₃]$^{16-}$	545	3.1	44	4
[b][(SiW₉O₃₄)₂Co₈(OH)₆(H₂O)₂(CO₃)₃]$^{16-}$	1436	10	29	4
[c][Co₅^{II}Co₂^{III}(mdea)₄(N₃)₂(CH₃CN)₆(OH)₂(H₂O)₂]$^{4-}$	88	1.75	24	98
[d][Co₄(H₂O)₂(PW₉O₃₄)₂]$^{10-}$	75	5	64	99
[e][Co₆(H₂O)₃₀{Co₉Cl₂(OH)₃(H₂O)₉(SiW₈O₃₁)₃}]$^{5-}$	100	0.042	—	100
[f][{Co₂Sb₂(H₂O)₁₀(B-β-(SbW₉O₃₃)}₂]$^{4-}$	193	5.3	31	18
[{β-SiNi₂W₁₀O₃₆(OH)₂(H₂O)}₄]^{24}	335	1.7	27	77

^{a} 2 μM cat., borate buffer (80 mM, pH 9). ^{b} 0.5 μM cat., borate buffer (80 mM, pH 9). ^{c} 25 μM cat., borate buffer (0.2 M, pH 8). ^{d} [Ru(bpy)₃]$^{3+}$ used as oxidant. ^{e} 1.27 μM cat., borate buffer (80 mM, pH 8). ^{f} 4 μM cat., borate buffer (80 mM, pH 8.5).

WOC test with the same concentration of cobalt centers was performed for cobalt acetate (40 μM based on Co), and the obtained 54% O_2 yield was lower compared to **Co(1)**.

Recycling experiments showed further activity of the catalytic system after adding additional $Na_2S_2O_8$ and adjusting the pH back to 8. The 2nd and 3rd cycle showed O_2 yields of 25% and 11%, respectively (Table S14 and Fig. S36†). Throughout the recycling, a continuous color change was observed from bright orange to dark green, suggesting a slow decomposition of the photosensitizer $[Ru(bpy)_3]^{2+}$. This shows that low photosensitizer stability associated with the formation of sulfate radicals from $Na_2S_2O_8$ are the main reasons for the decline of O_2 evolution.

CoNi(2) showed reduced photocatalytic oxygen evolution performance compared to pure **Co(1)**. O_2 yields decreased from 63% to 26% at a catalyst concentration of 40 μM (Table 1). The calculated O_2 yield per Co center (for 40 μM catalyst) is 16% for **Co(1)** and 15% for **CoNi(2)**, respectively. This underscores further that the Ni centers are most likely inactive. Our previous work on the molecular cubane water oxidation catalyst $[Co_4(dpy-C\{OH\}O)_4(OAc)_2(H_2O)_2](ClO_4)_2$ showed a comparable trend towards lower O_2 yields upon introducing Ni into the cobalt sites. This may imply that an intramolecular O–O coupling pathway between two Co–OH_n ligands prevails for O_2 evolution from such oxocluster WOCs, as reported for Co_3O_4.[97] **CoNi(2)** furthermore displays a larger band gap (2.66 eV) than **Co(1)** (2.41 eV, see Fig. S7 and S8†).

The expected formation of a solid POM–PS complex was observed after the catalytic O_2 evolution tests.[101] FT-IR analysis shows the presence of both photosensitizer and **Co(1)** in the precipitate (Fig. 5). For the POM–PS complex, characteristic bands are observed at 989, 939 ($\nu_{as}W–O_d$) and 874 cm^{-1} ($\nu_{as}W–O_b$) compared to 980, 932 and 884 cm^{-1} for the pristine **Co(1)**. Additional, three bands at 1463, 1444 and 1423 cm^{-1} can be attributed to $[Ru(bpy)_3]^{2+}$, in line with previous reports on POM–PS complex formation.[102]

This precipitation is a general phenomenon of POM-WOCs in such photocatalytic assays due to the electrostatic interactions between negatively charged POMs and positively charged photosensitizer molecules. Only at low catalyst concentrations <2 μM no measureable precipitation was detected, although such amounts most likely fall below the detection limit of frequently used DLS devices. Note that those devices were designed to quantify size distribution of large amounts of nanoparticles rather than for evidencing their absence.[103]

Further EDX analyses of the POM–PS complex show a homogeneous distribution of Ru, Co and W and calculated ratios of 2.5 : 1 $[Ru(bpy)_3]^{2+}$: **Co(1)** (Table S4,† based on the N : W ratio, Fig. S22†). Notably, lyophilisation of the remaining solution showed no presence of cobalt, which further supports that **Co(1)** does not undergo leaching of Co^{2+} ions into the solution (Fig. S21†). A subsequent WOC test with the filtered solution and additional $Na_2S_2O_8$ showed no further activity (Fig. S37†).

Photocatalytic tests with the recovered POM–PS complex, revealed its continuous activity with 34% O_2 yield, which is superior to the direct recycling run of the pristine POM in solution. This shows that the POM–PS complex is still active as a catalyst and that the photocatalytic assay ($[Ru(bpy)_3]^{2+}$/ $Na_2S_2O_8$) causes the fast decline of O_2 formation for pristine **Co(1)**.

3.2.2 Electrocatalytic activity of Co(1) and CoNi(2). Fig. 6 displays the results of electrocatalytic activity tests, where the onset potentials for **Co(1)** and **CoNi(2)** were determined as 0.96 V and 1.00 V *vs.* Ag/AgCl, respectively. The higher onset potential of **CoNi(2)** corresponds to the lower photocatalytic water oxidation performance. According to previous reports, Co-based POM electrocatalysts can undergo Co^{2+} leaching, especially in basic conditions.[104] The leached Co^{2+} ions can then form an active heterogeneous CoO_x film on the working electrode and contribute to the WOC activity.[30] During several CV scans, **Co(1)** and **CoNi(1)** showed minor shifts of the onset potential and anodic peaks to lower potentials (0.08 V after 3 cycles, Fig. S38 and S39†), which might be attributed to such CoO_x formation on the working electrode. It is of note that the Pt counter electrode was tested in the applied potential range and showed no activity (see blank measurements below). Previous reports showed dissolution and re-deposition of Pt on
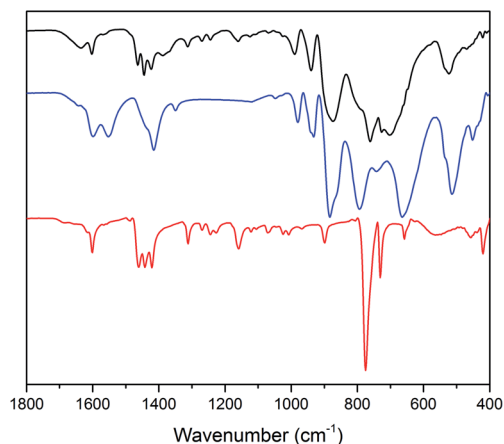

Fig. 5 FT-IR spectra of the **Co(1)**–POM–PS complex (black), pristine **Co(1)** (blue) and $[Ru(bpy)_3]Cl_2$ (red).

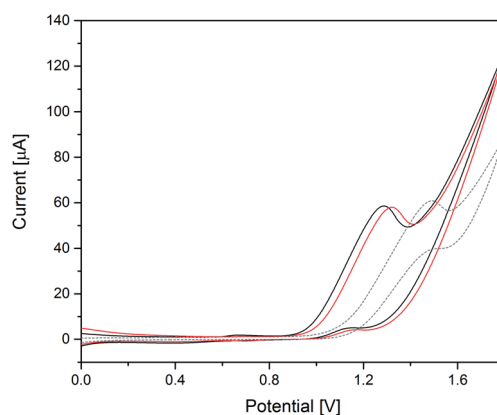Fig. 6 Cyclic voltammograms of 50 μM **Co(1)** (black) and 50 μM **CoNi(2)** (red) in 0.1 M borate buffer pH 8 and blank measurements (grey, dashed; V *vs.* Ag/AgCl, scan rate: 20 mV s^{-1}, 3rd scan is shown).

the reduction half-cell in acidic reaction media.[105] To the best of our knowledge, no such influence of Pt electrodes has been reported for the OER before.[106]

3.3. Co(1) and CoNi(2) as precursors for heterogeneous WOCs

Next, the heterogeneous tungstate WOCs emerging from **Co(1)** and **CoNi(2)** as precursors were investigated for their electrocatalytic performance.

The significant influence of the annealing temperature is quite evident from the cyclic voltammetry results (Fig. 7). Amorphous **CoW300** has an onset potential of 0.79 V *vs.* Ag/AgCl in borate buffer (0.1 M, pH 8) solution and maintains its catalytic performance over the measured eight cycles.

A broad cathodic peak at 0.55 V can be seen in the backward scan, which moves slowly to higher potentials in the subsequent scans (0.07 V during eight cycles, *cf.* Fig. S47†). The amorphous sample shows constant catalytic performance over several cycles

Fig. 7 Top: Cyclic voltammograms of **CoW300** (red), **CoW400** (blue) and **CoW500** (green); bottom: CVs of **CoNi300** (red), **CoNi400** (blue) and **CoNi500** (green); all measurements on FTO in 0.1 M borate buffer pH 8 *vs.* blank measurements (black, dashed; V *vs.* Ag/AgCl, scan rate: 20 mV s^{-1}, 3rd scan is shown).

with stable anodic and cathodic peaks. Previously reported amorphous $CoWO_4$ showed a substantial change in the anodic and cathodic peak after the first cycle.[66]

The onset potential of the crystalline samples **CoW400** and **CoW500** gradually increases to 0.94 V and 1.18 V *vs.* Ag/AgCl, respectively (Fig. S45†). This is in line with previous observations for amorphous and crystalline $CoWO_4$ and their onset potentials.[68,69] Interestingly, the onset potential of **CoW500** is almost the same as of the blank FTO electrode.

The onset potentials for the Ni-doped analogues are shifted to higher potentials (Fig. 7). Other than the pure Co samples, the onset potential values for **CoNi300** and **CoNi400** are closer, namely 0.91 V and 0.98 V, respectively (Fig. S46†). On the other hand, **CoNi500** has a better onset potential (1.08 V) compared to its binary analogue **CoW500** (1.18 V).

As mentioned above, the blue shift of the {WO_4} Raman peak of **CoW300** suggests a reduced distance between Co^{2+} ions, which can further influence the mechanism of the electrocatalytic water oxidation.[66,92] This was previously reported and confirmed with EXAFS analyses for amorphous and crystalline $CoWO_4$,[33] where the outstanding performance of the amorphous $CoWO_4$ was attributed to the shorter Co–Co distances.

Although the water oxidation reaction is a complex process, it was reported in previous studies that its mechanism strongly depends on the distance between the active sites of heterogeneous electrocatalysts.[33] Along these lines, it is assumed that closer intermetallic distances in the range of the O–O bond distance of dioxygen are favoring the "dual-site" Langmuir–Hinshelwood (LH) mechanism. In this mechanism, oxygen species are first adsorbed on adjacent sites, followed by their formation of molecular oxygen. In the case of longer distances between the active metal sites, however, the "single-site" Eley–Rideal (ER) mechanism may take place instead.

The dual-site LH mechanism requires a lower overpotential than the single-site ER mechanism, because the latter includes the formation of a peroxo intermediate at the single active metal center. This is considered a thermodynamically less favorable step for the overall water oxidation.[66,107] In the present case, the observed decrease of the Co–Co distances in **CoW300** may therefore facilitate the bridging of two terminal oxo groups to generate dioxygen *via* the LH mechanism.[66,108] This agrees with the observed lowest onset potential for **CoW300** among the tungstate catalyst series.

CoW300 as best performing member of the tungstate series was further compared to a reference sample obtained from a conventional solution co-precipitation method (annealed at 300 °C) for $CoWO_4$ and to RuO_2 as a well-established benchmark WOC (Fig. 8).[66] **CoW300** showed a lower onset potential (0.79 V) than the as-synthesized reference sample (0.84 V).

Furthermore, chronoamperometry measurements of **CoW300** and the conventionally synthesized reference material were performed. The superior performance of **CoW300** is clearly evident from the lower Tafel slope (inset Fig. 8) of 96 mV dec^{-1}, compared to 144 mV dec^{-1} for the reference material obtained from Na_2WO_4 and $Co(NO_3)_2$.[66]
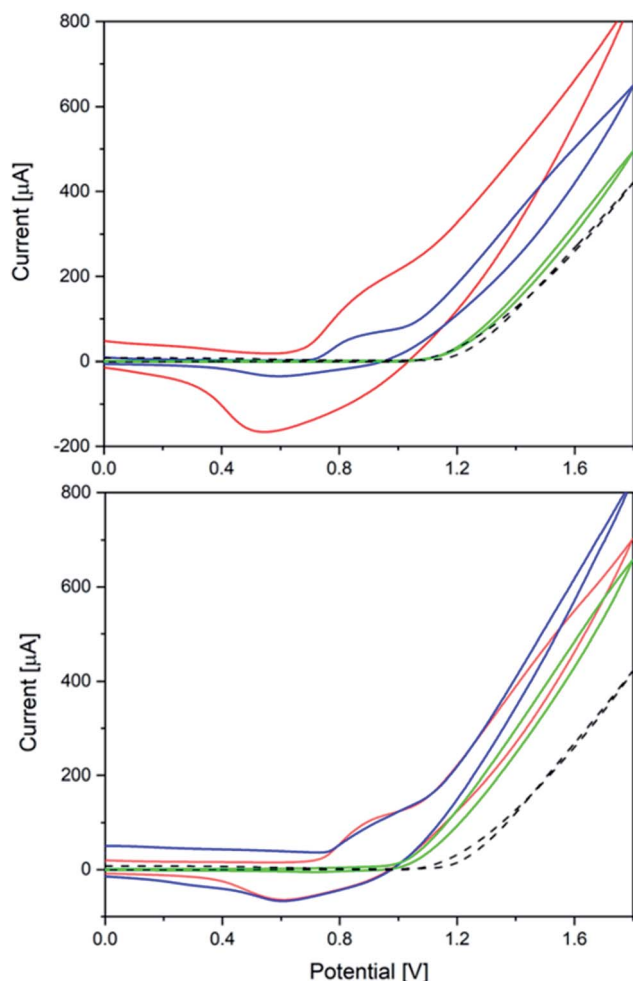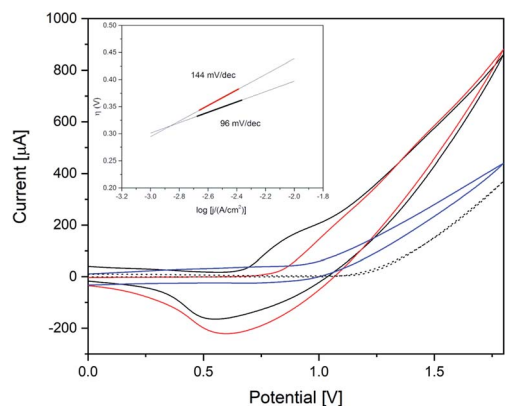
Fig. 8 Cyclic voltammograms of **CoW300** (black); CoWO$_4$ (red); RuO$_2$ (blue) and reference FTO (dotted) in 0.1 M borate buffer pH 8 (scan rate: 20 mV s^{-1}); inset: Tafel plot of **CoW300** (black) and CoWO$_4$ (red).

4.   Conclusions

A bio-inspired polyoxometalate with an open Co$_4$-core architecture, K$_5$Na$_3$[(A-α-SiW$_9$O$_{34}$)Co$_4$(OH)$_3$(CH$_3$COO)$_3$] **Co(1)**, was synthesized as a model system to investigate crucial questions of water oxidation catalyst (WOC) design, namely (1) the controversially discussed effect of Co/Ni-synergisms in molecules *vs.* solids, (2) the influence of preparative history and precursor choice on WOC activity and (3) the role of amorphous features in solid WOC performance.

First, the open Co$_4$-POM **Co(1)** displayed competitive photocatalytic activity with an oxygen yield of 63% for the optimal catalyst concentration of 40 μM. Furthermore, its new mixed Co/Ni isostructural analogue **CoNi(2)** was synthesized, analyzed and tested for water oxidation activity. Co/Ni substitution did not exert a productive influence on the water oxidation activity of the mixed-metal POMs, in contrast to widely reported Co/Ni synergisms in solid WOCs.

Next, to investigate the effect of mixed metal molecular precursors on cobalt tungstate-related WOCs as attractive target materials, **Co(1)** and **CoNi(2)** were subjected to thermal treatment. Both compounds afforded CoWO$_4$- as well as (Co, Ni) WO$_4$-related phases with increasing degrees of crystallinity upon higher annealing temperatures.

Concerning the influence of crystallinity on the performance, cyclic voltammetry measurements clearly showed that amorphous **CoW300** obtained from annealing **Co(1)** at 300 °C showed the lowest onset potential among both series of tungsten oxides obtained from POM precursors. Most importantly, **CoW300** displayed a lower onset potential than a representative reference sample of CoWO$_4$ that was synthesized *via* a conventional co-precipitation/annealing method.

In line with the catalytic trends for the **Co(1)** and **CoNi(2)** precursor POMs, introduction of nickel centers did not exert a productive effect on the heterogeneous tungstate catalysts either. This is in stark contrast to the growing number of literature reports on Co/Ni synergisms in a wide range of oxide and non-oxide heterogeneous electrocatalysts. Further systematic studies are now required to understand the dependence of

such metal–metal interactions on the catalyst matrix and its preparative history, as well as on the applied performance test conditions.

Our results demonstrate that readily accessible POMs are promising precursors with pre-organized metal centers for the convenient synthesis of amorphous heterogeneous water oxidation catalysts, which outperform products of conventional high temperature approaches starting from simple binary educts. Interestingly, neither the molecular precursors nor their heterogeneous WOC products were responsive to widely employed synergistic Co/Ni doping strategies. This highlights the complexity and matrix dependence of such mixed metal optimization strategies, which are in the focus of forefront catalytic endeavours.

To fully transfer the tunable potential of polynuclear molecular precursors into high performance amorphous catalysts with optimal near-range order properties, in-depth monitoring and theoretical studies of mixed metal interactions in different settings are now required.

Conflicts of interest

There are no conflicts of interest to declare.

Acknowledgements

References

1 I. Roger, M. A. Shipman and M. D. Symes, *Nat. Rev. Chem.*, 2017, **1**, 0003.

2 N.-T. Suen, S.-F. Hung, Q. Quan, N. Zhang, Y.-J. Xu and H. M. Chen, *Chem. Soc. Rev.*, 2017, **46**, 337–365.

3 Y. Umena, K. Kawakami, J.-R. Shen and N. Kamiya, *Nature*, 2011, **473**, 55–60.

4 F. Song, K. Al-Ameed, M. Schilling, T. Fox, S. Luber and G. R. Patzke, *J. Am. Chem. Soc.*, 2019, **141**, 8846–8857.

5 J. Wei, Y. Feng, P. Zhou, Y. Liu, J. Xu, R. Xiang, Y. Ding, C. Zhao, L. Fan and C. Hu, *ChemSusChem*, 2015, **8**, 2630–2634.

6 F. Evangelisti, R. Güttinger, R. Moré, S. Luber and G. R. Patzke, *J. Am. Chem. Soc.*, 2013, **135**, 18734–18737.

7 G. C. Dismukes, R. Brimblecombe, G. A. N. Felton, R. S. Pryadun, J. E. Sheats, L. Spiccia and G. F. Swiegers, *Acc. Chem. Res.*, 2009, **42**, 1935–1943.

8 B. Gao, T. Wang, Y. Li, X. Fan, H. Gong, C. Jiang, P. Li, X. Huang and J. He, *Chem. Commun.*, 2020, **56**, 4244–4247.

9 S. Tandon, J. Soriano-López, A. C. Kathalikkattil, G. Jin, P. Wix, M. Venkatesan, R. Lundy, M. A. Morris, G. W. Watson and W. Schmitt, *Sustainable Energy Fuels*, 2020, **4**, 4464–4468.

10 A. Dey, V. Kumar, S. Pal, A. Guha, S. Bawari, T. N. Narayanan and V. Chandrasekhar, *Dalton Trans.*, 2020, **49**, 4878–4886.

11 (*a*) Q. Yin and C. L. Hill, *Nat. Chem.*, 2018, **10**, 6–7; (*b*) W. Liu, W. Mu, M. Liu, X. Zhang, H. Cai and Y. Deng, *Nat. Commun.*, 2014, **5**, 3208; (*c*) H. G. T. Ly, G. Absillis, R. Janssens, P. Proost and T. N. Parac-Vogt, *Angew. Chem., Int. Ed. Engl.*, 2015, **54**, 7391–7394; (*d*) F. Lucarini, M. Pastore, S. Vasylevskyi, M. Varisco, E. Solari, A. Crochet, K. M. Fromm, F. Zobi and A. Ruggi, *Chem.–Eur. J.*, 2017, **23**, 6768–6771.

12 D. Gao, I. Trentin, L. Schwiedrzik, L. González and C. Streb, *Molecules*, 2019, **25**, 157–177.

13 (*a*) Y. V. Geletii, B. Botar, P. Kögerler, D. A. Hillesheim, D. G. Musaev and C. L. Hill, *Angew. Chem., Int. Ed.*, 2008, **47**, 3896–3899; (*b*) A. Sartorel, M. Carraro, G. Scorrano, R. de Zorzi, S. Geremia, N. D. McDaniel, S. Bernhard and M. Bonchio, *J. Am. Chem. Soc.*, 2008, **130**, 5006–5007; (*c*) G. Zhu, Y. V. Geletii, P. Kögerler, H. Schilder, J. Song, S. Lense, C. Zhao, K. I. Hardcastle, D. G. Musaev and C. L. Hill, *Dalton Trans.*, 2012, **41**, 2084–2090.

14 D. Nesterov and O. Nesterova, *Catalysts*, 2018, **8**, 602.

15 Q. Han and Y. Ding, *Dalton Trans.*, 2018, **47**, 8180–8188.

16 X.-B. Han, C. Qin, X.-L. Wang, Y.-Z. Tan, X.-J. Zhao and E.-B. Wang, *Appl. Catal., B*, 2017, **211**, 349–356.

17 X.-B. Han, D.-X. Wang, E. Gracia-Espino, Y.-H. Luo, Y.-Z. Tan, D.-F. Lu, Y.-G. Li, T. Wågberg, E.-B. Wang and L.-S. Zheng, *Chin. J. Catal.*, 2020, **41**, 853–857.

18 Q. Han, D. Sun, J. Zhao, X. Liang and Y. Ding, *Chin. J. Catal.*, 2019, **40**, 953–958.

19 J. Lin, X. Meng, M. Zheng, B. Ma and Y. Ding, *Appl. Catal., B*, 2019, **241**, 351–358.

20 S. D. Adhikary, A. Tiwari, T. C. Nagaiah and D. Mandal, *ACS Appl. Mater. Interfaces*, 2018, **10**, 38872–38879.

21 F. Lucarini, J. Fize, A. Morozan, M. Marazzi, M. Natali, M. Pastore, V. Artero and A. Ruggi, *Sustainable Energy Fuels*, 2020, **4**, 589–599.

22 F. Song, Y. Ding, B. Ma, C. Wang, Q. Wang, X. Du, S. Fu and J. Song, *Energy Environ. Sci.*, 2013, **6**, 1170–1184.

23 K. Fan, H. Chen, B. He and J. Yu, *Chem. Eng. J.*, 2020, **392**, 123744.

24 S. Bae, H. Kim, D. Jeon and J. Ryu, *ACS Appl. Mater. Interfaces*, 2019, **11**, 7990–7999.

25 W. Fang, R. Tao, Z. Jin, Z. Sun, F. Li and L. Xu, *J. Alloys Compd.*, 2019, **797**, 140–147.

26 Y. Choi, D. Jeon, Y. Choi, D. Kim, N. Kim, M. Gu, S. Bae, T. Lee, H.-W. Lee, B.-S. Kim and J. Ryu, *ACS Nano*, 2019, **13**, 467–475.

27 L. Zhang, X. Ding, M. Cong, Y. Wang and X. Zhang, *Int. J. Hydrogen Energy*, 2019, **44**, 9203–9209.

28 X. Cao, Y. Wang, J. Lin and Y. Ding, *J. Mater. Chem. A*, 2019, **7**, 6294–6303.

29 R. Al-Oweini, A. Sartorel, B. S. Bassil, M. Natali, S. Berardi, F. Scandola, U. Kortz and M. Bonchio, *Angew. Chem., Int. Ed.*, 2014, **53**, 11182–11185.

30 J. Stracke and R. G. Finke, *J. Am. Chem. Soc.*, 2011, **133**, 14872–14875.

31 (*a*) J. J. Stracke and R. G. Finke, *ACS Catal.*, 2013, **3**, 1209–1219; (*b*) S. Goberna-Ferrón, J. Soriano-López, J. R. Galán-Mascarós and M. Nyman, *Eur. J. Inorg. Chem.*, 2015, **2015**, 2833–2840.

32 K. P. Sullivan, M. Wieliczko, M. Kim, Q. Yin, D. L. Collins-Wildman, A. K. Mehta, J. Bacsa, X. Lu, Y. V. Geletii and C. L. Hill, *ACS Catal.*, 2018, **8**, 11952–11959.

33 Y. Han, K. Choi, H. Oh, C. Kim, D. Jeon, C. Lee, J. H. Lee and J. Ryu, *J. Catal.*, 2018, **367**, 212–220.

34 S. Suseno, C. C. L. McCrory, R. Tran, S. Gul, J. Yano and T. Agapie, *Chem.–Eur. J.*, 2015, **21**, 13420–13430.

35 J. Pfrommer, A. Azarpira, A. Steigert, K. Olech, P. W. Menezes, R. F. Duarte, X. Liao, R. G. Wilks, M. Bär, T. Schedel-Niedrig and M. Driess, *ChemCatChem*, 2017, **9**, 672–676.

36 R. Deshmukh and M. Niederberger, *Chem.–Eur. J.*, 2017, **23**, 8542–8570.

37 L. Warmuth, C. Ritschel and C. Feldmann, *RSC Adv.*, 2020, **10**, 18377–18383.

38 L. Warmuth and C. Feldmann, *ACS Omega*, 2019, **4**, 13400–13407.

39 A. L. Luna, F. Matter, M. Schreck, J. Wohlwend, E. Tervoort, C. Colbeau-Justin and M. Niederberger, *Appl. Catal., B*, 2020, **267**, 118660.

40 (*a*) X. Xing, Y. Gui, G. Zhang and C. Song, *Electrochim. Acta*, 2015, **157**, 15–22; (*b*) F. Ahmadi, M. Rahimi-Nasrabadi, A. Fosooni and M. Daneshmand, *J. Mater. Sci.: Mater. Electron.*, 2016, **27**, 9514–9519; (*c*) K. Adib, M. Rahimi-Nasrabadi, Z. Rezvani, S. M. Pourmortazavi, F. Ahmadi, H. R. Naderi and M. R. Ganjali, *J. Mater. Sci.: Mater. Electron.*, 2016, **27**, 4541–4550.

41 L. Reith, K. Lienau, D. S. Cook, R. Moré, R. I. Walton and G. R. Patzke, *Chem.–Eur. J.*, 2018, **24**, 18424–18435.

42 L. Reith, K. Lienau, C. A. Triana, S. Siol and G. R. Patzke, *ACS Omega*, 2019, **4**, 15444–15456.

43 K. Lienau, C. A. Triana, L. Reith, S. Siol and G. R. Patzke, *Front. Chem.*, 2020, **8**, 473.

44 Y.-H. Lai, C.-Y. Lin, Y. Lv, T. C. King, A. Steiner, N. M. Muresan, L. Gan, D. S. Wright and E. Reisner, *Chem. Commun.*, 2013, **49**, 4331–4333.

45 X.-B. Han, X.-Y. Tang, Y. Lin, E. Gracia-Espino, S.-G. Liu, H.-W. Liang, G.-Z. Hu, X.-J. Zhao, H.-G. Liao, Y.-Z. Tan, T. Wagberg, S.-Y. Xie and L.-S. Zheng, *J. Am. Chem. Soc.*, 2019, **141**, 232–239.

46 P. Beato, A. Blume, F. Girgsdies, R. E. Jentoft, R. Schlögl, O. Timpe, A. Trunschke, G. Weinberg, Q. Basher, F. A. Hamid, S. B. A. Hamid, E. Omar and L. Mohd Salim, *Appl. Catal., A*, 2006, **307**, 137–147.

47 S. Bommineni, M. D. Skoglund, A. R. Morris, E. J. Doskocil and J. H. Holles, *Appl. Catal., A*, 2013, **467**, 202–210.

48 Y. Huang, Y. Sun, X. Zheng, T. Aoki, B. Pattengale, J. Huang, X. He, W. Bian, S. Younan, N. Williams, J. Hu, J. Ge, N. Pu,

X. Yan, X. Pan, L. Zhang, Y. Wei and J. Gu, *Nat. Commun.*, 2019, **10**, 982.

49 Y. Huang, J. Ge, J. Hu, J. Zhang, J. Hao and Y. Wei, *Adv. Energy Mater.*, 2018, **8**, 1701601.

50 J.-S. Li, Y. Wang, C.-H. Liu, S.-L. Li, Y.-G. Wang, L.-Z. Dong, Z.-H. Dai, Y.-F. Li and Y.-Q. Lan, *Nat. Commun.*, 2016, **7**, 11204.

51 Y. Zhao, W. Wan, Y. Chen, R. Erni, C. A. Triana, J. Li, C. K. Mavrokefalos, Y. Zhou and G. R. Patzke, *Adv. Energy Mater.*, 2020, 2002228.

52 L. Zhang, Q. Fan, K. Li, S. Zhang and X. Ma, *Sustainable Energy Fuels*, 2020, **4**, 5417–5432.

53 L. Lei, D. Huang, M. Cheng, R. Deng, S. Chen, Y. Chen and W. Wang, *Coord. Chem. Rev.*, 2020, **418**, 213372.

54 S. M. Jasem and A. C. C. Tseung, *J. Electrochem. Soc.*, 1979, **126**, 1353–1360.

55 (*a*) R. P. Antony, A. K. Satpati, K. Bhattacharyya and B. N. Jagatap, *Adv. Mater. Interfaces*, 2016, **3**, 1600632; (*b*) I. Abidat, C. Morais, C. Comminges, C. Canaff, J. Rousseau, N. Guignard, T. W. Napporn, A. Habrioux and K. B. Kokoh, *J. Mater. Chem. A*, 2017, **5**, 7173–7183; (*c*) H. Shi and G. Zhao, *J. Phys. Chem. C*, 2014, **118**, 25939–25946; (*d*) R. Chen, H.-Y. Wang, J. Miao, H. Yang and B. Liu, *Nano Energy*, 2015, **11**, 333–340.

56 Y. Yang, H. L. Fei, G. D. Ruan, C. S. Xiang and J. M. Tour, *ACS Nano*, 2014, **8**, 9518–9523.

57 A. QayoomMugheri, A. Tahira, U. Aftab, M. IshaqAbro, S. R. Chaudhry, L. Amaral and Z. H. Ibupoto, *Electrochim. Acta*, 2019, **306**, 9–17.

58 J. W. Nai, H. J. Yin, T. T. You, L. R. Zheng, J. Zhang, P. X. Wang, Z. Jin, Y. Tian and J. Z. Liu, *Adv. Energy Mater.*, 2015, **5**, 1401880.

59 L. Wang, C. Lin, D. K. Huang, F. X. Zhang, M. K. Wang and J. Jin, *ACS Appl. Mater. Interfaces*, 2014, **6**, 10172–10180.

60 R. D. L. Smith, M. S. Prévot, R. D. Fagan, S. Trudel and C. P. Berlinguette, *J. Am. Chem. Soc.*, 2013, **135**, 11580–11586.

61 Y. Tang, H. Yang, J. Sun, M. Xia, W. Guo, L. Yu, J. Yan, J. Zheng, L. Chang and F. Gao, *Nanoscale*, 2018, **10**, 10459–10466.

62 R. Wu, B. Xiao, Q. Gao, Y.-R. Zheng, X.-S. Zheng, J.-F. Zhu, M.-R. Gao and S.-H. Yu, *Angew. Chem., Int. Ed.*, 2018, **57**, 15445–15449.

63 R. J. Müller, J. Lan, K. Lienau, R. Moré, C. A. Triana, M. Iannuzzi and G. R. Patzke, *Dalton Trans.*, 2018, **47**, 10759–10766.

64 F. Song, R. Moré, M. Schilling, G. Smolentsev, N. Azzaroli, T. Fox, S. Luber and G. R. Patzke, *J. Am. Chem. Soc.*, 2017, **139**, 14198–14208.

65 S. Zhang, Q. Xing and W.-H. Sun, *RSC Adv.*, 2016, **6**, 72170–72176.

66 H. Jia, J. Stark, L. Q. Zhou, C. Ling, T. Sekito and Z. Markin, *RSC Adv.*, 2012, **2**, 10874–10881.

67 C. Ling, L. Q. Zhou and H. Jia, *RSC Adv.*, 2014, **4**, 24692–24697.

68 A. Indra, P. W. Menezes, N. R. Sahraie, A. Bergmann, C. Das, M. Tallarida, D. Schmeißer, P. Strasser and M. Driess, *J. Am. Chem. Soc.*, 2014, **136**, 17530–17536.

69 D. Chen, C.-L. Dong, Y. Zou, D. Su, Y.-C. Huang, L. Tao, S. Dou, S. Shen and S. Wang, *Nanoscale*, 2017, **9**, 11969–11975.

70 M. W. Kanan and D. G. Nocera, *Science*, 2008, **321**, 1072–1075.

71 S. L. González-Cortés, T.-C. Xiao, P. M. Costa, S. M. Rodulfo-Baechler and M. L. Green, *J. Mol. Catal. A: Chem.*, 2005, **238**, 127–134.

72 V. Srirapu, A. Kumar, P. Srivastava, R. N. Singh and A. Sinha, *Electrochim. Acta*, 2016, **209**, 75–84.

73 B. Huang, H. Wang, S. Liang, H. Qin, Y. Li, Z. Luo, C. Zhao, L. Xie and L. Chen, *Energy Storage Mater.*, 2020, **32**, 105–114.

74 A. S. Rajpurohit, N. S. Punde, C. R. Rawool and A. K. Srivastava, *Chem. Eng. J.*, 2019, **371**, 679–692.

75 S. M. El-Sheikh and M. M. Rashad, *J. Cluster Sci.*, 2015, **26**, 743–757.

76 X.-B. Han, Y.-G. Li, Z.-M. Zhang, H.-Q. Tan, Y. Lu and E.-B. Wang, *J. Am. Chem. Soc.*, 2015, **137**, 5486–5493.

77 L. Yu, Y. Ding, M. Zheng, H. Chen and J. Zhao, *Chem. Commun.*, 2016, **52**, 14494–14497.

78 L. Lisnard, P. Mialane, A. Dolbecq, J. Marrot, J. M. Clemente-Juan, E. Coronado, B. Keita, P. de Oliveira, L. Nadjo and F. Sécheresse, *Chem.–Eur. J.*, 2007, **13**, 3525–3536.

79 A. P. Ginsberg, *Inorganic Syntheses*, John Wiley & Sons, Inc, Hoboken, NJ, USA, 1990.

80 C. Rocchiccioli-Deltcheff, M. Fournier, R. Franck and R. Thouvenot, *Inorg. Chem.*, 1983, **22**, 207–216.

81 J. Niu, Z. Wang and J. Wang, *J. Coord. Chem.*, 2004, **57**, 1271–1277.

82 R. Thouvenot, M. Fournier, R. Franck and C. Rocchiccioli-Deltcheff, *Inorg. Chem.*, 1984, **23**, 598–605.

83 F. Song, K. Al-Ameed, M. Schilling, T. Fox, S. Luber and G. R. Patzke, *J. Am. Chem. Soc.*, 2019, **141**, 8846–8857.

84 F. Song, R. Moré, M. Schilling, G. Smolentsev, N. Azzaroli, T. Fox, S. Luber and G. R. Patzke, *J. Am. Chem. Soc.*, 2017, **139**, 14198–14208.

85 C. Pichon, P. Mialane, A. Dolbecq, J. Marrot, E. Rivière, B. S. Bassil, U. Kortz, B. Keita, L. Nadjo and F. Sécheresse, *Inorg. Chem.*, 2008, **47**, 11120–11128.

86 T. Montini, V. Gombac, A. Hameed, L. Felisari, G. Adami and P. Fornasiero, *Chem. Phys. Lett.*, 2010, **498**, 113–119.

87 S. J. Naik and A. V. Salker, *Solid State Sci.*, 2010, **12**, 2065–2072.

88 T.-D. Nguyen, C.-T. Dinh and T.-O. Do, *Nanoscale*, 2011, **3**, 1861–1873.

89 T. You, G. Cao, X. Song, C. Fan, W. Zhao, Z. Yin and S. Sun, *Mater. Lett.*, 2008, **62**, 1169–1172.

90 P. K. Pandey, N. S. Bhave and R. B. Kharat, *J. Mater. Sci.*, 2007, **42**, 7927–7933.

91 R. L. Moreira, R. M. Almeida, K. P. F. Siqueira, C. G. Abreu and A. Dias, *J. Phys. D: Appl. Phys.*, 2015, **49**, 45305.

92 Q. Chen, T.-W. Huang, M. Baldini, A. Hushur, V. Pomjakushin, S. Clark, W. L. Mao, M. H. Manghnani,

A. Braun and T. Graule, *J. Phys. Chem. C*, 2011, **115**, 24021–24027.

93 V. K. Malinovsky, V. N. Novikov, N. V. Surovtsev and A. P. Shebanin, *Phys. Solid State*, 2000, **42**, 65–71.

94 S. Fukuzumi, J. Jung, Y. Yamada, T. Kojima and W. Nam, *Chem.–Asian J.*, 2016, **11**, 1138–1150.

95 H. Lv, Y. V. Geletii, C. Zhao, J. W. Vickers, G. Zhu, Z. Luo, J. Song, T. Lian, D. G. Musaev and C. L. Hill, *Chem. Soc. Rev.*, 2012, **41**, 7572–7589.

96 X.-B. Han, Z.-M. Zhang, T. Zhang, Y.-G. Li, W. Lin, W. You, Z.-M. Su and E.-B. Wang, *J. Am. Chem. Soc.*, 2014, **136**, 5359–5366.

97 S. Koroidov, M. F. Anderlund, S. Styring, A. Thapper and J. Messinger, *Energy Environ. Sci.*, 2015, **8**, 2492–2503.

98 J.-H. Xu, L.-Y. Guo, H.-F. Su, X. Gao, X.-F. Wu, W.-G. Wang, C.-H. Tung and D. Sun, *Inorg. Chem.*, 2017, **56**, 1591–1598.

99 Q. Yin, J. M. Tan, C. Besson, Y. V. Geletii, D. G. Musaev, A. E. Kuznetsov, Z. Luo, K. I. Hardcastle and C. L. Hill, *Science*, 2010, **328**, 342–345.

100 M. Natali, I. Bazzan, S. Goberna-Ferrón, R. Al-Oweini, M. Ibrahim, B. S. Bassil, H. Dau, F. Scandola, J. R. Galán-Mascarós, U. Kortz, A. Sartorel, I. Zaharieva and M. Bonchio, *Green Chem.*, 2017, **19**, 2416–2426.

101 P.-E. Car, M. Guttentag, K. K. Baldridge, R. Alberto and G. R. Patzke, *Green Chem.*, 2012, **14**, 1680–1688.

102 F. Evangelisti, P.-E. Car, O. Blacque and G. R. Patzke, *Catal. Sci. Technol.*, 2013, **3**, 3117–3129.

103 J. Li, R. Güttinger, R. Moré, F. Song, W. Wan and G. R. Patzke, *Chem. Soc. Rev.*, 2017, **46**, 6124–6147.

104 S. J. Folkman, J. Soriano-Lopez, J. R. Galán-Mascarós and R. G. Finke, *J. Am. Chem. Soc.*, 2018, **140**, 12040–12055.

105 (*a*) R. Chen, C. Yang, W. Cai, H.-Y. Wang, J. Miao, L. Zhang, S. Chen and B. Liu, *ACS Energy Lett.*, 2017, **2**, 1070–1075; (*b*) P. P. Lopes, D. Strmcnik, D. Tripkovic, J. G. Connell, V. Stamenkovic and N. M. Markovic, *ACS Catal.*, 2016, **6**, 2536–2544.

106 S. Cherevko, A. R. Zeradjanin, G. P. Keeley and K. J. J. Mayrhofer, *J. Electrochem. Soc.*, 2014, **161**, H822–H830.

107 Y.-H. Fang and Z.-P. Liu, *J. Am. Chem. Soc.*, 2010, **132**, 18214–18222.

108 L.-P. Wang and T. van Voorhis, *J. Phys. Chem. Lett.*, 2011, **2**, 2200–2204.